



HAL
open science

Two-dimensional snapshot measurement of surface variation of anchoring in liquid crystal cells

Eleni Perivorali, Giampaolo d'Allessandro, Vasilis Apostolopoulos, Nicolas Brouckaert, Thomas Heiser, Malgosia Kaczmarek

► **To cite this version:**

Eleni Perivorali, Giampaolo d'Allessandro, Vasilis Apostolopoulos, Nicolas Brouckaert, Thomas Heiser, et al.. Two-dimensional snapshot measurement of surface variation of anchoring in liquid crystal cells. *Liquid Crystals*, 2021, 48 (15), pp.2086-2096. 10.1080/02678292.2021.1928309 . hal-03797709

HAL Id: hal-03797709

<https://hal.science/hal-03797709>

Submitted on 16 Sep 2024

HAL is a multi-disciplinary open access archive for the deposit and dissemination of scientific research documents, whether they are published or not. The documents may come from teaching and research institutions in France or abroad, or from public or private research centers.

L'archive ouverte pluridisciplinaire **HAL**, est destinée au dépôt et à la diffusion de documents scientifiques de niveau recherche, publiés ou non, émanant des établissements d'enseignement et de recherche français ou étrangers, des laboratoires publics ou privés.



Distributed under a Creative Commons Attribution - NonCommercial - NoDerivatives 4.0 International License



Two-dimensional snapshot measurement of surface variation of anchoring in liquid crystal cells

Eleni Perivolari, Giampaolo D'Alessandro, Vasilis Apostolopoulos, Nicolas Brouckaert, Thomas Heiser & Malgosia Kaczmarek

To cite this article: Eleni Perivolari, Giampaolo D'Alessandro, Vasilis Apostolopoulos, Nicolas Brouckaert, Thomas Heiser & Malgosia Kaczmarek (2021) Two-dimensional snapshot measurement of surface variation of anchoring in liquid crystal cells, *Liquid Crystals*, 48:15, 2086-2096, DOI: [10.1080/02678292.2021.1928309](https://doi.org/10.1080/02678292.2021.1928309)

To link to this article: <https://doi.org/10.1080/02678292.2021.1928309>



© 2021 The Author(s). Published by Informa UK Limited, trading as Taylor & Francis Group.



Published online: 25 May 2021.



Submit your article to this journal [↗](#)



Article views: 1601



View related articles [↗](#)



View Crossmark data [↗](#)



Citing articles: 5 View citing articles [↗](#)

Two-dimensional snapshot measurement of surface variation of anchoring in liquid crystal cells

Eleni Perivolari ^a, Giampaolo D'Alessandro ^b, Vasilis Apostolopoulos ^a, Nicolas Brouckaert^a, Thomas Heiser ^c and Malgosia Kaczmarek^a

^aPhysics and Astronomy, University of Southampton, Southampton, UK; ^bMathematical Sciences, University of Southampton, Southampton, UK; ^cLaboratoire ICube, Université de Strasbourg, CNRS, UMR 7357, Strasbourg, France

ABSTRACT

Enhanced, photoactive response can be realised by integrating liquid crystals with photoalignment or photoconductive alignment layers. Such cells, asymmetric by design, need to be monitored for the stability and uniformity, especially in the regions exposed to light. In this work, we report on an integrated, versatile model and technique to characterise their core parameters as well as more subtle effects, such as the strength of anchoring energy. The snapshot method also provides two-dimensional maps of the cells' thickness, pretilt angle and uniformity.

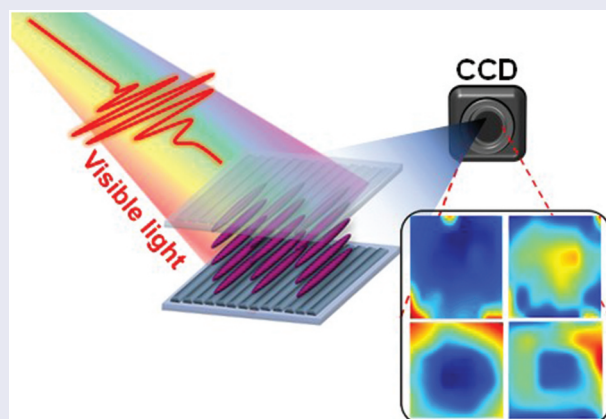
ARTICLE HISTORY

Received 28 January 2021

Accepted 6 May 2021

KEYWORDS

Nematic liquid crystals; photoactive materials; anchoring energy; measurements of elastic constants; 2D imaging



1. Introduction

Photoaddressable command layers for liquid crystals (LCs) with photoconductive [1–4], photoalignment [5–8] and, more recently photovoltaic layers [9–12], promise new application areas of LCs, e.g. in telecommunications and organic electronics. They also offer an increased level of control, such as the contactless LC alignment provided by photoalignment. This avoids the deposition of charge or dust on the substrates caused by rubbing. Moreover, it can be applied to either assembled or disassembled cells [8], the former being impossible for many other LC alignment methods, due to the mechanical inaccessibility of bulk regions. However, the photosensitivity of the cell command layers can also cause the pretilt and anchoring to change in the regions exposed to optical or electric fields [8,13,14]. This is particularly relevant for photoaligned LC cells, as the

strength of anchoring can depend on the duration of light exposure [8,15]. There is, thus, a need for a quick and comprehensive characterisation technique and model to be able to map the uniformity of the cells, and their pretilts and anchoring energy on both surfaces, as well as monitor any changes with time or illumination.

There are many different methods reported in the literature to measure individual properties of LC cells. For example, their thickness and uniformity can be obtained by the wave retarder rotational method [16] or by the phase compensation method (PCM) [17]. The pretilt angle can be characterised by spectroscopic ellipsometry [18] or the crystal rotation method [19]. The measurement of the anchoring energy relies on various techniques, such as the light-scattering [20], the wedge-cell [21], the retardation vs. voltage (RV) methods [22],

CONTACT Eleni Perivolari  E.Perivolari@soton.ac.uk

© 2021 The Author(s). Published by Informa UK Limited, trading as Taylor & Francis Group.

This is an Open Access article distributed under the terms of the Creative Commons Attribution-NonCommercial-NoDerivatives License (<http://creativecommons.org/licenses/by-nc-nd/4.0/>), which permits non-commercial re-use, distribution, and reproduction in any medium, provided the original work is properly cited, and is not altered, transformed, or built upon in any way.

electrical measurements [23], as well as a reflective method [24]. Several of these experimental methods can only work if the LCs are placed in specially prepared cells and are not well suited to characterise more advanced LC devices, with different or multiple layers on the substrates [25]. All of them address one single spot on the surface of the cell, or they assume that the cell has uniform properties.

To address these issues and obtain quick and reliable estimates of a gamut of LC parameters, allows us to interactively determine, from a single measurement and in real time, a range of LC and cell parameters. The particular strength of our method is that it can capture, at the same time, the parameters that strongly influence the response of LCs to external fields, such as elastic constants, viscosity, cell thickness, pretilt, as well as weaker and finer parameters, such as the strength of polar anchoring. While subtle, polar anchoring plays a major role in applications, for example bistable displays [26], e-books [27], and biological sensors [28]. It is also at the heart of the new LC physics of particle-like LC configurations, like skyrmions and torons [29], that can form complex topological structures.

In this paper we build on our previous work [30,31] and extend it in two directions that are suitable to new LC devices and physics. First, we use the whole cell measurements to estimate the average polar anchoring energy. The second development direction addresses one of the defining features of modern photosensitive cells: they are often asymmetric, with different alignment layers (ALs) on the input and output facet. Here, we are restricted to planar nematic LCs, but in principle, our method can be adapted to other LC alignments.

The structure of this paper is as follows. In the next section, we summarise the mathematical model used to fit the experimental CPI traces and extract the LC and cell parameters. The experimental procedure is described in Section 3. The two-dimensional measurements of thickness and pretilt in symmetric and asymmetric cells are the topic of the following Section, 4. The measurement of the anchoring energy and its validation is the topic of Section 5. The paper is concluded by a discussion of all the measurements in Section 6, followed by a summary of our findings and an outline of further areas of work.

2. Model of asymmetric cells, code implementation and validation

The strength of the model for the characterisation lies in its integrated, comprehensive approach to simultaneously extract the main parameters. We model the LC alignment in the planar nematic cell using the

Frank-Oseen theory [30,32]. We neglect the LC fluid motion, since only smoothly varying high-frequency voltages are applied to the LC when measuring the CPI. The ALs are parallel to the (x_1, x_2) -coordinate plane, while the x_3 axis is into the cell. We assume that the cell lateral variations are large with respect to the LC relaxation length so that the director n is a function only of the coordinate into the cell, n . We parameterise the LC orientation by the tilt angle $\theta(x_3)$, that the director field forms with the ALs. With this notation we can write the director field as,

$$n = [\cos(\theta), 0, \sin(\theta)]. \quad (1)$$

The equation for the alignment of the LC cell takes the form [33]:

$$\gamma_1 \frac{\partial \theta}{\partial t} = \frac{\partial}{\partial x_3} \left[\frac{K_1}{2} [1 + \cos(2\theta)] + \frac{K_3}{2} [1 - \cos(2\theta)] \right] \frac{\partial \theta}{\partial x_3} + \frac{1}{2} \sin(2\theta) \left[(K_1 - K_3) \left(\frac{\partial \theta}{\partial x_3} \right)^2 + \epsilon_0 \epsilon_A \left(\frac{\partial \psi}{\partial x_3} \right)^2 \right] \quad (2)$$

where γ_1 is the LC rotational viscosity, K_1 and K_3 are the splay and bend elastic constants respectively, ϵ_0 is the vacuum permittivity, $\epsilon_A = \epsilon_{\parallel} - \epsilon_{\perp}$ is the dielectric anisotropy of the nematic LC, with ϵ_{\parallel} and ϵ_{\perp} the component of dielectric permittivity tensor parallel and perpendicular to the director, respectively.

The electrostatic potential $\psi(x_3)$ is given by the first of Maxwell's equations, which, in this geometry, can be written as:

$$\frac{d}{dx_3} \left[\left(1 + \frac{\epsilon_A}{\epsilon_{\perp}} \sin^2[\theta(x_3)] \right) \frac{d}{dx_3} \psi(x_3) \right] = 0. \quad (3)$$

This can be solved explicitly [30,31] as:

$$\psi(x_3) = \int_0^{x_3} \frac{V}{1 + \frac{\epsilon_A}{\epsilon_{\perp}} \sin^2[\theta(\xi_3)]} d\xi_3 \left[\int_0^L \frac{1}{1 + \frac{\epsilon_A}{\epsilon_{\perp}} \sin^2[\theta(x_3)]} dx_3 \right]^{-1}, \quad (4)$$

where V is the possibly time dependent, rms voltage applied to the cell and L is the cell thickness. The Rapini-Papoular [34] alignment conditions on Equation (2) are:

$$+ \left[\frac{K_1}{2} [1 + \cos(2\theta)] + \frac{K_3}{2} [1 - \cos(2\theta)] \right] \frac{\partial \theta}{\partial x_3} = \frac{W_L}{2} \sin[2(\theta - \theta_0(0))], \quad (5)$$

$$- \left[\frac{K_1}{2} [1 + \cos(2\theta)] + \frac{K_3}{2} [1 - \cos(2\theta)] \right] \frac{\partial \theta}{\partial x_3} = \frac{W_R}{2} \sin[2(\theta - \theta_0(L))], \quad (6)$$

at $x_3 = 0$ and $x_3 = L$ respectively. In these equations $\theta_0(0)$ and $\theta_0(L)$ are the AL preferred alignment direction at $x_3 = 0$ and $x_3 = L$ respectively. Similarly, W_L and W_R are the surface polar anchoring energy coefficients at $x_3 = 0$ and $x_3 = L$ respectively.

Lastly, we define the CPI to be the ratio between the output and input intensity, so that it is normalised in the interval $[0,1]$. Hence, the CPI is given by:

$$I(V) = \sin^2 \left(\frac{\pi L}{\lambda_0} [n_0 - n_{\text{eff}}(\theta(x_3))] dx_3 \right) \quad (7)$$

where $n_{\text{eff}}(\theta)$ is the effective refractive index seen by the component of polarisation in the plane of the director,

$$n_{\text{eff}}(\theta) = \frac{n_e n_o}{\sqrt{n_o^2 \cos^2(\theta) + n_e^2 \sin^2(\theta)}}. \quad (8)$$

Here, n_o and n_e are the optical ordinary and extraordinary refractive indices, respectively.

The model in Equation (2) has been integrated numerically in MATLAB using a spectral collocation method to discretise space [35], and an implicit variable step algorithm (MATLAB routine ode15s) to integrate in time. The solution of the electrostatic equation, Equation (4), and the CPI integral in Equation (7) were computed using a Clencurt quadrature [35]. The boundary condition Equations (5) and (6) are solved using an approximate solution in the limit of very strong or very weak anchoring or using a Newton solver for the director at the boundary in all intermediate cases. The code was validated by successfully comparing its results with the output of a finite element implementation of the model in COMSOL Multiphysics. The alignment Equation (2) was implemented as a General Form PDE with a boundary flux source given by Equations (5) and (6), while the electrostatic Equation (3) is solved numerically using the Electrostatic module. We have not used the analytical solution of this equation, given by Equation (4), to ensure that the two codes were maximally independent.

3. Experimental methodology

The measurements were performed with the aid of a fully packaged and bespoke optical setup that we call the Optical Multi-Parameter Analyser (OMPA). It performs a computer-controlled cross-polarised intensity (CPI) measurements and real-time data analysis and fitting. For the fitting process, prior information about a set of complementary LC parameters, namely dielectric coefficients, and refractive indices, of the LC material is required. This is typically provided on LC specification sheets. In order to verify the validity of our method, we measured three different LC cells that cover a range of LCs and ALs. Two of these samples were symmetric, i.e. with the same AL on both substrates ($\text{AL}_x\text{-LC-AL}_x$), while the third type was asymmetric, i.e. with different ALs ($\text{AL}_x\text{-LC-AL}_y$). In asymmetric cells in which one substrate is known, it is possible to use this method to estimate the pretilt and anchoring energy of the unknown substrate.

Initially, a standard, reference LC cell was prepared consisting of the nematic LC E7 and two glass substrates coated with ITO conductive layers and with rubbed polyimide (PI), to produce an anti-parallel planar alignment of the LC (see Figure 1(a)). This technique ensures a uniform planar alignment inside the cell without defects and twist deformations. The substrates had size 2×2 cm and were held together with UV-cured glue. The thickness of LC layer was controlled by $6 \mu\text{m}$ spacers. The cells were filled through capillary forces with the LC in the isotropic phase and sealed along the perimeter of the cell. The choice of LC layer was driven by the availability in the literature of its physical, electrical, and optical properties so that we could benchmark our measurements and results.

As a counterpart to the standard LC nematic material and ALs (E7 and PI) used in the first test system that is known to have relatively strong anchoring energy, the second test cells included a less well-known LC mixture and AL. We used a LC with low reorientation voltage threshold, QYTN-004 from Qingdao QY Liquid

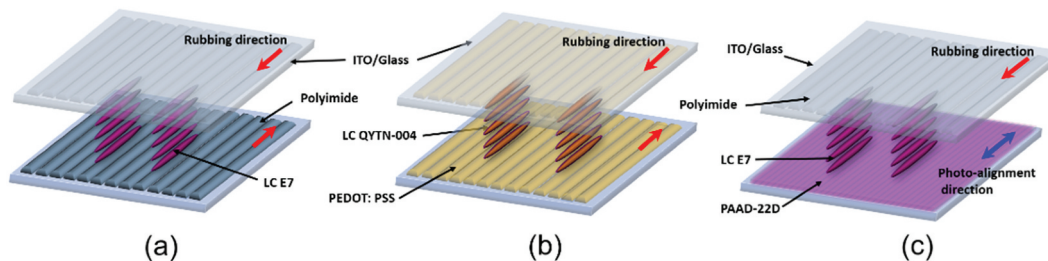


Figure 1. (Colour online) Sample schematics. (a) Planar symmetric E7 cell where both ALs are rubbed PI (PI-E7-PI). (b) Planar symmetric QYTN-004 cell, where both ALs are rubbed PEDOT: PSS (PEDOT: PSS-QYTN004-PEDOT: PSS). (c) Planar asymmetric E7 cell, where one AL is rubbed PI while the other is photoaligned PAAD-22D (PI-E7-PAAD22D).

Crystal Co. The two identical ALs consist of a conductive polymer poly(3,4-ethylenedioxythiophene) polystyrene sulphonate, PEDOT:PSS (commercial name CPP105D) as AL, coated over ITO glass substrates. The sample area was 1×1 cm, and the thickness of LC was set by $6 \mu\text{m}$ spacers (see Figure 1(b)). PEDOT:PSS is a popular material used as an electrode in both the cells with flexible substrates [36,37] and in the cells with photovoltaic layers [38,39].

Finally, our third sample was an asymmetric LC cell. For reliability, we kept the nematic E7 as LC layer and PI as one of the ALs. The other was coated with a photoaligning azobenzene dye (PAAD-22D) provided by the Beam Co (see Figure 1(c)). PAAD materials were demonstrated as effective for LC alignment by one-step illumination with visible light [26]. To control the thickness of the LC layer we used $7 \mu\text{m}$ spacers. For clarity, Table 1 summarises the specifications of the experimental samples.

The OMPA characterises LC devices by measuring the CPI across the whole cell area as a function of the frequency and voltage amplitude applied to the cell. It provides the capability to capture a snapshot of the LC device with its ALs and determine its key properties. The experimental apparatus is shown in Figure 2. A light beam from a fibre coupled diode laser is launched through a fibre port connector which collimates the beam. Two lenses (L1 and L2) expand and collimate the beam in order to cover a wide area of the

cell (diameter ~ 1 cm). In this paper we have used a laser wavelength of 642 nm , but other wavelengths can easily be selected by attaching a different laser to the fibre port. The sample is located between two crossed polarisers, each at 45° to the director alignment, and the light enters at normal incidence. After propagating through the cell, the light beam is collected by a CCD camera. Data from neighbouring pixels are averaged so that the image collected has effective pixels of approximately one millimetre in size. Over the 10 cm distance between the cell and the detector, diffraction expands the effective pixel diameter by less than 10%. Therefore, to a good approximation the CCD camera acts as a spatial resolution detector and each effective pixel corresponds to a single spot in the surface of the cell, allowing us to draw maps of the cell thickness, pretilt angle and of the anchoring energy. When the two polarisation components of the incident light pass through the cell, they experience different phase delays that are function of the LC alignment. We change this by applying an AC voltage to the cell and measure the CPI as a function of it. We monitor the power of the laser before and after the cell using two beam splitters to redirect a fraction of the beam intensity to two photodiodes. Finally, the entire setup is enclosed to reduce the background noise to the detectors and CCD camera and thermal fluctuations. If needed, it is possible to enclose the LC cell in a temperature stabilised holder. This was not required for the measurements reported here, but it is essential when studying temperature effects on the LC parameters.

The experiment is fully managed by a MATLAB code [40,41], which controls the measuring apparatus, data acquisition and performs the data analysis using the model described in Section 2 [30]. OMPA collects pointwise data across the cell and fits the elastic constants, the pretilt angle, the anchoring energy, and the cell thickness.

Table 1. Description of the samples.

Experimental samples	LC material	AL 1	AL 2	Thickness (d), [μm]
Symmetric cell 1	E7	PI	PI	6
Symmetric cell 2	QYTN-004	PEDOT: PSS	PEDOT: PSS	6
Asymmetric cell 1	E7	PI	PAAD22D	7

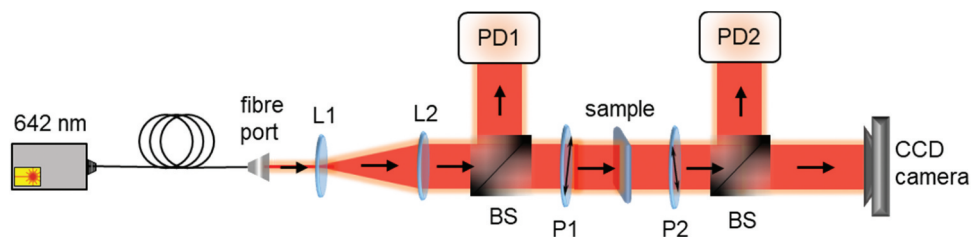


Figure 2. (Colour online) Experimental setup of the OMPA instrument. A fibre coupled diode laser at 642 nm passes from a fibre port into two lenses L1 and L2 which expand and collimate the beam. The sample is located between two crossed polarisers (P1 and P2), each at 45° to the director alignment, where the light enters at normal incidence. Photodiodes, PD1 and PD2 monitor the power of the laser before and after the cell by exploiting two beam splitters (BS). Finally, the light is incident on a CCD camera, which we use as spatial resolution detector. The entire setup is enclosed to reduce the background noise to the detectors and CCD camera and reduce thermal fluctuations.

The fitting procedure is as follows. The cell thickness, pretilt, splay elastic constant and anchoring energy are fitted using the part of the CPI trace between 0 V and the first extremum. We then keep the cell thickness and pretilt fixed and fit all the other parameters using the entire trace. We use the MATLAB function `lsqcurvefit` to minimise the distance between the experimental and numerical CPI traces. The fitting of multiple traces is done in a similar manner [30,31].

The quality of the fit is determined by visual inspection of the traces (see Figure 4 for an example) and by estimating the error bars on the liquid crystal parameters, e.g. the elastic constants, that are measured at multiple locations (see Ref [30,31]) for a detailed error analysis of the measurement process. We have also verified the impact of potential errors in the values of the LC dielectric permittivities and refractive indices. A 1% variation of any of these parameters produces changes in the fitted parameters by at most, 2%. In principle the OMPA can also detect a set of Leslie viscosities, but we do not demonstrate this feature in this paper since it is included in our previous work [31].

The software graphical user interface allows us also to set the range of AC voltages and specify the region of the cell surface where the measurements are to be taken. In our experiment, the CPI as a function of voltage is measured by applying a 10 kHz AC voltage to the LC cell and ramping the voltage peak-to-peak amplitude from 0 to 20 V in incremental steps of 0.1 V. OMPA experimental apparatus is straightforward. It is seamlessly connected to the accompanying integrated model and code (described in Section 2), which in spite of its complexity, outputs the fitted parameters in clear and easy to follow way. Thus, the monitoring for any changes can be easily achieved.

4. Mapping anchoring, pretilt and thickness LC cells

We have analysed $3.5 \times 3.5 \text{ mm}^2$, and $7 \times 7 \text{ mm}^2$ areas of the two symmetric cells, PI – E7 (Figure 3(a,b)) and PEDOT: PSS – QYTN-004 (Figure 3(c,d)), respectively. This translates into 5×5 and 8×6 points measured across the cell along the x and y axis. The spatial

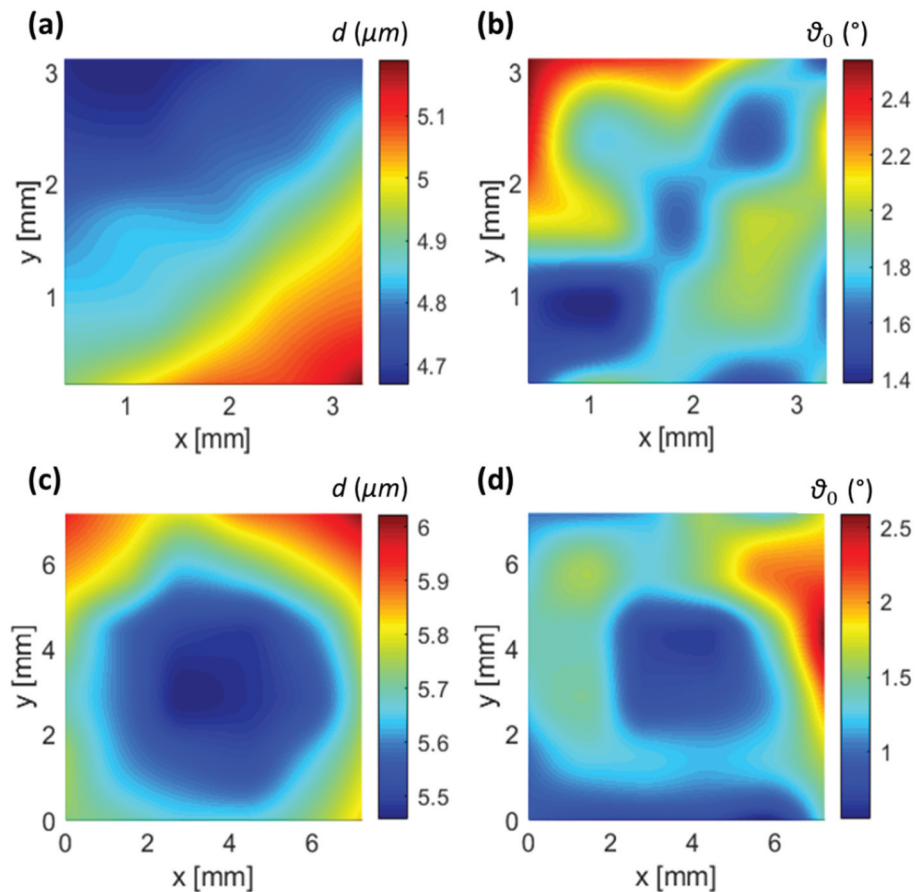


Figure 3. (Colour online) Spatial maps of thickness and pretilt angle of symmetric cells: (a) thickness and (b) pretilt angle maps of PI – E7 cell. (c) thickness and (d) pretilt angle maps of PEDOT: PSS – QYTN-004 cell.

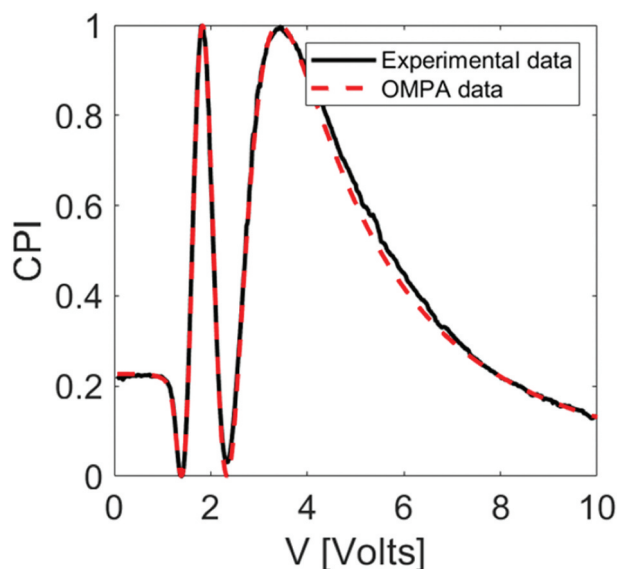


Figure 4. (Colour online) CPI trace for the asymmetric PI – PAAD-22D planar cell filled with E7. Parameter values: $K_1 = 11$ pN, $K_3 = 16.4$ pN, $\epsilon_{\parallel} = 19.54$, $\epsilon_{\perp} = 5.17$, $d = 7$, $\theta_{PAAD} = 0.34^\circ$, $\theta_{PI} = 1.9^\circ$, $W_{PAAD} = 0.21$ mJ/m², $W_{PI} > 1000$ mJ/m², $\lambda = 642$ nm, $n_e = 1.7287$ and $n_o = 1.5182$.

resolution emerged from the 25 sampling spots, is 0.7 mm along x and y axis, while for the 48 sampling spots, is 0.88 mm along the x-axis and 1.2 mm along the y-axis. These measurements show that the cell surface parameters, like the pretilt angle, vary over a millimetre scale, much larger than the LC relaxation length. This allows us to consider each sample point in the cell as independent from its neighbours and, hence, to apply the model derived in Section 2 to each of them individually.

Typical maps of the thickness and the pretilt angle of the PI-E7-PI cell are shown in Figure 3(a,b). Here, we capture the edge of the cell where clearly thickness variation can be seen. The cell is thinner in the centre and thicker at the edges with a variation of 0.5 μ m and average of 4.9 μ m. This is most likely due to the excess of pressure applied in the centre of the cell when sealing the edges. The fact that the LC thickness varies, highlights not only the difficulty on fabricating uniform LC cells, but also the importance of mapping the thickness profile. A similar behaviour is displayed by the thickness map of symmetric PEDOT: PSS – QYTN-004 sample (Figure 3(c)). The cell is thinner in the centre and thicker at the edges, with a variation between 5.5 and 6 μ m and average of 5.7 μ m. These data should be compared with the spacer size used in these cells which is 6 μ m for both samples.

The pretilt angle map of E7 (Figure 3(b)) has an average value of $1.89^\circ \pm 0.06^\circ$, while Figure 3(d) presents the pretilt map of PEDOT: PSS – QYTN-004.

A visual inspection of this cell showed that the alignment was only correct at the central part of the cell. This is confirmed by this pretilt map: in the inner region the pretilt is very uniform with an average value of $1.28^\circ \pm 0.08^\circ$. Outside this region, both the pretilt value and, more importantly, its fluctuations are larger, reflecting the poor visual quality of the cell there.

The CPI trace responds only to the average alignment properties of the cell. It is however possible to use it in an asymmetric cell, provided that one layer has already been characterised with the same LC as the one used in the asymmetric cell. Briefly, for an asymmetric LC measurement (AL_x-LC-AL_y), we fix the pretilt angle and anchoring energy of the known layer AL_x and fit those of the unknown layer AL_y. This process is completely automated by the OMPA software. As it is ultimately a subtraction measurement, the error in this procedure is intrinsically higher than for a symmetric cell, but it allows the analysis of cells where one layer has to be different from the other, e.g. photovoltaic cells [42].

The asymmetric cell that we tested here, is a PI – E7 – PAAD-22D (Figure 1(c)) where the known layer AL_x is a standard rubbed PI and the layer to be fitted, AL_y, is a photoaligning azobenzene dye layer. In this example we extracted the optical parameters for PI from the symmetric cell PI – E7, that we measured earlier (Figure 3(a,b)). In Figure 5, we present maps of the cell thickness and of the PAAD layer pretilt. Both maps are very uniform, with few exceptions in specific points close to the boundaries. The average thickness (Figure 5(a)) is $6.55 \mu\text{m} \pm 0.01$, while average pretilt (Figure 5(b)) is $0.16^\circ \pm 0.02^\circ$. Essentially, the spatial variations (Figure 5(a,b)) occur due to fabrication imperfections at the right-side edge of the cell. PAAD-22D is aligned using a 450 nm laser [26]. In order to keep the intensity sufficiently high we could not expand the beam to an area larger than approximately 7 mm in diameter.

5. Anchoring energy

5.1 The effect of the anchoring energy

In principle, the polar anchoring energy affects the alignment of the LC at all values of the voltage applied to the cell, and its strength can be deduced from the changes in LC reorientation with increasing electric field. Small values of the anchoring energy weaken the LC molecule binding to the AL, thus making it easier for the electric field to tilt the molecular axis. However, for intermediate values of the anchoring energy we expect that the binding to the AL layer will be weakened mainly at large voltage values. In this case, the LC axis is parallel

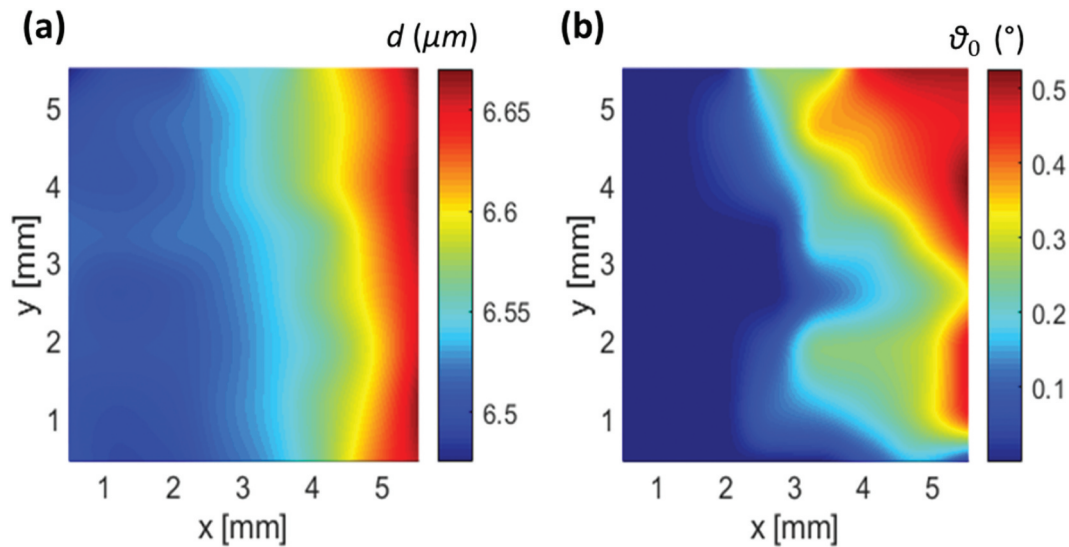


Figure 5. (Colour online) Asymmetric PI – PAAD-22D planar cell filled with E7: spatial map of the LC (a) thickness and (b) pretilt angle.

to the electric field across most of the cell and there is a considerable bending of the director field near the cell sides that strains the molecular attachment to the surface thus amplifying the effect of not having an infinitely strong anchoring. We can verify this by comparing CPI traces computed for four different values of the anchoring energy, logarithmically spaced between $10 \mu\text{J}/\text{m}^2$ and $10 \text{ mJ}/\text{m}^2$ a range that stretches from very weak to very strong anchoring (see Figure 6). The difference between the three largest values of the anchoring energy is insignificant at low voltage, while it is well visible at high voltage, especially if the anchoring is not too strong. It is only when the anchoring is very weak that the low voltage region is affected.

5.2 Minimisation landscapes

It is clear that the anchoring energy has an effect on the CPI and so, in principle, it should be possible to determine its value by fitting experimental CPI traces. In practice, however, its effect is small and so it may not be possible to determine its value accurately. For example, in the specific case of the traces in Figure 6, it is immediately clear that even a minimal amount of noise would make the traces that correspond to anchoring energy of $10 \text{ mJ}/\text{m}^2$ and $1 \text{ mJ}/\text{m}^2$ indistinguishable. In other words, the stronger the anchoring, the harder it is to obtain an accurate measure [22,23].

Another factor that can contribute to the poor quality of a parameter measurement, even if the fit is excellent, is the presence of degeneracies between parameters. This is a well-known problem in parameter fitting. To check whether fitting the anchoring energy is possible, i.e. to verify that there are no

quasi-degeneracies, we have inspected the minimisation landscape around a known solution. We have fixed a set of LC and cell parameters, indicated by a superscript 0, as in $K_1^{(0)}$, $K_3^{(0)}$, etc., and have computed the corresponding CPI trace, $I(V_j; K_1^{(0)}, K_3^{(0)}, d^{(0)}, \theta_0^{(0)}, W^{(0)})$, where V_j is the j -th voltage value at which the CPI trace is evaluated, $\theta_0^{(0)}$ indicates the common value of the two pretilt angles and $W^{(0)}$ the common value of the two anchoring energies (we assume for simplicity that the cell is symmetric). We have then varied two parameters, for example the bend elastic constant and the anchoring energy, and computed the corresponding CPI trace, $I(V_j; K_1^{(0)}, K_3, d^{(0)}, \theta_0^{(0)}, W)$. Finally, we have computed the distance between the two traces,

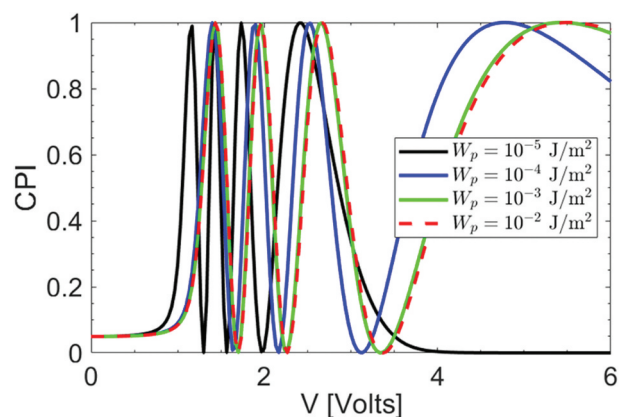


Figure 6. (Colour online) CPI traces for different values of the anchoring energy in a symmetric cell. Parameter values: $K_1 = 10.9 \text{ pN}$, $K_3 = 17.9 \text{ pN}$, $\epsilon_{\parallel} = 19.54$, $\epsilon_{\perp} = 5.17$, $d = 12$, $\theta = 2^\circ$, $\lambda = 642 \text{ nm}$, $n_e = 1.7287$ and $n_o = 1.5182$.

$$D(K_3, W) = \sum_{j=1}^N \left[I(V_j; K_1^{(0)}, K_3^{(0)}, d^{(0)}, \theta_0^{(0)}, W^{(0)}) - I(V_j; K_1^{(0)}, K_3, d^{(0)}, \theta_0^{(0)}, W) \right]^2 \quad (9)$$

where N is the total number of voltage values used. This is the function that is minimised when fitting the LC parameters, in this case the bend elastic constant and the anchoring energy at the two sides of the symmetric cell. Parameters are independent if $D(K_3^{(0)}, W^{(0)})$ is an isolated minimum. We have plotted the distance, Equation (9), as function of three different combinations of parameters in Figure 7, forming minimisation landscapes. The anchoring energy (W) is along the horizontal axis and varies by $\pm 30\%$ with respect to $W^{(0)}$. The vertical axes are, from left to right, the splay and bend elastic energy, and the pretilt angle. In all cases there is an isolated minimum, confirming that the anchoring energy can indeed be fitted. The region of the minimum in the left and in the middle of the plots is elongated, indicating that the estimate on the anchoring energy can be changed significantly just by a relatively small change in either of the elastic energies. The region of the minimum in the rightmost plot, instead, is more symmetric indicating that the pretilt and the anchoring energy are to a good approximation independent one of the other. The minimisation landscapes offer only a local analysis of the best fit, as is the case for the covariance matrix method to estimate correlations between parameters. It is always possible that there may be other local minima in the landscape, especially when varying all the parameters. We try to avoid this pitfall of all high-dimension minimisation methods by repeating the fitting of the experimental CPI traces using different initial guesses of the fitting parameters.

In summary, this analysis shows that it is possible, in principle and in practice, to fit the polar anchoring energy values from the very weak to strong regime. The precision of the fit may be affected by errors in the estimates of the elastic energy coefficients; the more precisely these are known, the more accurate the estimate of the anchoring energy will be. If the LC system is in a very strong anchoring regime, the accurate value cannot be extracted, but in fact, this is not a significant limitation. In this regime the LC alignment is, by definition, not sensitive to the accurate value of the anchoring energy.

5.3 Polar anchoring energy experimental results

As discussed earlier, the polar anchoring energy effects are small and, hence, sensitive to noise in the measurement process. Moreover, they are mostly detectable in the large voltage amplitude part of the CPI trace. For these voltage values, most of the LC in the bulk is aligned with the electric field, and the only significant alignment variations are near the boundaries. Surface anomalies, like charge deposition, and dust, affect these measurements more significantly than those of the elastic constants, thickness and pretilt angle, whose value are related to the LC bulk properties, thus, adding to the noise on the measurement. To compensate for this, we have measured the polar anchoring energy averaged over the cell area. Our measurements are summarised in Table 2.

Table 2. Anchoring energy values from symmetric and asymmetric LC cells.

Measured LC cells	Average Polar Anchoring Energy on the photoactive layer [mJ/m ²]
Symmetric 1: PI-E7	> 1
Symmetric 2: PEDOT: PSS-QYTN-004	23 ± 11
Asymmetric 1: PI-E7- PAAD22D	0.26 ± 0.01

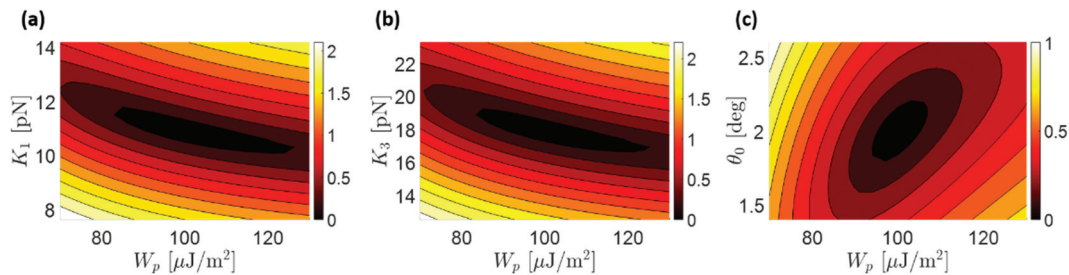


Figure 7. (Colour online) Minimisation landscapes: in all cases the anchoring energy is along the horizontal axis and varies by $\pm 30\%$ with respect to $W^{(0)}$. The vertical axes are, from left to right, the splay and bend elastic energy, and the pretilt angle. The scale of the colour bar is in arbitrary units. Parameter values: $K_1^{(0)} = 10.9$ pN, $K_3^{(0)} = 17.9$ pN, $\varepsilon_{\parallel} = 19.54$, $\varepsilon_{\perp} = 5.17$, $d^{(0)} = 12$, $\theta_0^{(0)} = 2^\circ$, $W^{(0)} = 100 \mu\text{J}/\text{m}^2$.

Table 3. Optical parameters of symmetric planar PI – E7 cell.

Source	K1 [pN]	K3 [pN]	Pretilt Angle [°]	Polar Anchoring Energy [mJ/m ²]
Literature	11.2 [43]	18.6 [43]	-	-
	10.8 [44]	17.5 [44]	-	-
	11.7 [45]	19.5 [45]	2 [45]	-
	11.5 [46]	18.2 [46]	-	-
	-	-	1.5 [47]	-
	-	-	-	0.3 [48]
	-	-	-	0.8 [49]
OMPA measurements	11.6 ± 0.2	17.8 ± 0.1	1.9 ± 0.1	1 [50]
				> 1

The average polar anchoring energy of the standard symmetric PI-E7 cell is >1 mJ/m², the upper bound of our detection window (see Figure 6). In the case of the complex LC mixture of QYTN-004 on PEDOT:PSS, the average polar anchoring energy is lower at 23 ± 11 mJ/m². In order to calculate the polar anchoring energy of the asymmetric PI – E7 – PAAD-22D cell, we exploited the optical parameters for PI from the symmetric cell PI – E7 (see Figure 3). The resulting average polar anchoring energy of E7 on PAAD-22D is 0.26 ± 0.01 mJ/m², a weaker alignment than on PI.

As the results in Table 2 demonstrates our method captured different anchoring strengths for a set of LC systems. Strong anchoring was measured for our reference cell (PI-E7), as expected, and a reduced anchoring was observed for the photoaddressable cells with photoalignment (PAAD) [15] and for a system with an organic conductor (PEDOT:PSS) [36]. While the anchoring is lower in those cells, it nevertheless remained in the regime associated with strong anchoring.

6. Discussion

The selection of a PI – E7 symmetric cell for our first set of measurements was driven by the availability of the E7 parameter values in the literature, making it the best candidate to calibrate the OMPA instrument. The literature parameter values together with those fitted by the OMPA are listed in Table 3. It is evident that even for this popular LC there are relatively few measurements, and none as comprehensive as those provided by the OMPA. As shown in Table 3, the OMPA measurements are in line with the literature ones. We also note that the spread

of values for the anchoring energy is quite significant, reflecting the difficulty in measuring this parameter.

The average measurements for QYTN-004 on PEDOT:PSS are summarised in Table 4. These are the first measurements we are aware of this low threshold voltage LC. Polar anchoring energy revealed a weaker behaviour than E7 on PI (23 ± 11 mJ/m²). This highlights the importance of being able to estimate the average value and fit both strong and weak anchoring energy responses, especially when characterising newly synthesised LC materials. In the case of the PI – PAAD-22D asymmetric cell, we have used the values listed in Table 3 to fix the alignment properties of E7 on PI and have fitted the pretilt angle and anchoring energy on the PAAD-22D side. The most surprising feature of this measurement is the relative weakness of the anchoring energy of E7 on PAAD-22D, with respect to PI (0.26 ± 0.01 mJ/m² and >1 mJ/m² respectively). Usually photoaligned azo-dye layers provide comparable anchoring energy with the rubbed LC alignment on PI [8,15,51].

This difference can be explained by non-optimum alignment of PAAD-22D layer, as observed in our earlier work [26]. The strength of anchoring at a photoalignment layer depends on the quality and uniformity of the film [51,52]. As shown here, the maps obtained for this cell indeed indicate some lack of uniformity. This is an additional, important feature of our method, i.e. that it is capable of detecting the lack of uniformity or stability over time, as commonly observed when dealing with new LC or alignment materials.

For azobenzene based PAAD ALs, the anchoring energy can be varied considerably by changing the UV exposure time and irradiation dose of azo-dyes [52]. In particular, the optimum anchoring energy is obtained when irradiation dose of a UV pump beam (365 nm) is higher than 1 J/cm² [53]. We have used a longer wavelength (450 nm) and a weaker irradiation dose (0.22 J/cm²). The second factor that affects the film quality is its thickness: very thin films may lack continuity and form islands. It is known that even very thin (e.g. 1 nm) layers of azo-dyes can be used to align LC, but with significantly reduced strength [15]. The thickness of the PAAD-22D layer in the asymmetric cell was estimated to be approximately 15 ± 10 nm, while it normally spans from 75 to 150 nm [54]. This larger thickness is likely to lead to smoother films with stronger anchoring.

Table 4. Experimental results of PEDOT: PSS – QYTN-004 cell.

Source	K1 [pN]	K3 [pN]	Pretilt Angle [°]	Polar Anchoring Energy [mJ/m ²]
OMPA measurements	10.08 ± 0.14	16.0 ± 0.4	1.28 ± 0.08	23 ± 11

7. Summary and conclusions

We have shown a fast, robust, reproducible, and accurate model and technique for characterising symmetric and asymmetric LC cells based on CPI measurements. This optical method can capture the subtle contribution

to the phase lag from anchoring on the substrates and use it to determine its strength when the dielectric anisotropy and birefringence of LC are known. We tested this approach on cells with a single photoalignment layer as well as on a system with organic conductors. In addition, the two-dimensional maps of uniformity of the cells were obtained, showing spatial variation of the thickness and of the pretilt angle, both important parameters for determining long-term stability of LC devices. Our measurements have focused on planar LC cells with voltage inactive layers. However, the technique we have presented can easily be extended to more complicated cell configurations. For example, including photoconductive or photovoltaic layers requires only to change Equation (4) in a relatively simple way, while modelling the effect of light-induced alignment changes requires only modest modifications of the boundary conditions Equations (5) and (6). This flexibility, coupled with the ease and speed of measurement, make our method an ideal tool for the characterisation of novel photoaddressable LC geometries.

Acknowledgments

The authors would like to thank Dr Nina Podoliak, Dr Oleksandr Buchnev, Eleanor White and Ben Beddoes for useful discussions.

Disclosure statement

No potential conflict of interest was reported by the author(s).

ORCID

Eleni Perivolari  <http://orcid.org/0000-0003-3051-7839>

Giampaolo D'Alessandro  <http://orcid.org/0000-0001-9166-9356>

Vasilis Apostolopoulos  <http://orcid.org/0000-0003-3733-2191>

Thomas Heiser  <http://orcid.org/0000-0003-0969-2034>

References

- [1] Kaczmarek M, Dyadyusha A, Slussarenko S, et al. The role of surface charge field in two-beam coupling in liquid crystal cells with photoconducting polymer layers. *J Appl Phys*. 2004;96(5):2616–2623.
- [2] Ono H, Kawatsuki N. Orientational holographic grating observed in liquid crystals sandwiched with photoconductive polymer films. *Appl Phys Lett*. 1997;71(9):1162–1164.
- [3] Huang BY, Huang SY, Chuang CH, et al. Electrically-tunable blue phase liquid crystal microlens array based on a photoconductive film. *Polymers*. 2020;12(1):65.
- [4] Kim HW, Choi KS, Mun J, et al. Photo-aligned and photo-conductive polymer layers for photorefractive liquid crystal cells of high transmittance. *Opt Mater*. 2003;21(1–3):657–662.
- [5] De Sio L, Klein G, Serak S, et al. All-optical control of localized plasmonic resonance realized by photoalignment of liquid crystals. *J Mater Chem C*. 2013;1(45):7483–7487.
- [6] Nersisyan S, Tabiryan N, Steeves DM, et al. Axial polarizers based on dichroic liquid crystals. *J Appl Phys*. 2010;108(3):033101.
- [7] Tsutsumi N. Recent advances in photorefractive and photoactive polymers for holographic applications. *Polym Int*. 2017;66(2):167–174.
- [8] Yaroshchuk O, Reznikov Y. Photoalignment of liquid crystals: basics and current trends. *J Mater Chem*. 2012;22(2):286–300.
- [9] Kumar M, Kumar S. Liquid crystals in photovoltaics: a new generation of organic photovoltaics. *Polym J*. 2017;49(1):85–111.
- [10] Bushby RJ, Lozman OR. Photoconducting liquid crystals. *Curr Opin Solid State Mater Sci*. 2002;6(6):569–578.
- [11] O'Neill M, Kelly SM. Liquid crystals for charge transport, luminescence, and photonics. *Adv Mater*. 2003;15(14):1135–1146.
- [12] Verbunt PP, Kaiser A, Hermans K, et al. Controlling light emission in luminescent solar concentrators through use of dye molecules aligned in a planar manner by liquid crystals. *Adv Funct Mater*. 2009;19(17):2714–2719.
- [13] Ouskova E, Reznikov Y, Shiyankovskii S, et al. Photo-orientation of liquid crystals due to light-induced desorption and adsorption of dye molecules on an aligning surface. *Phys Rev E*. 2001;64(5):051709.
- [14] Weng L, Liao PC, Lin CC, et al. Anchoring energy enhancement and pretilt angle control of liquid crystal alignment on polymerized surfaces. *AIP Adv*. 2015;5(9):097218.
- [15] Chigrinov V, Kwok HS, Takada H, et al. Photo-aligning by azo-dyes: physics and applications. *Liq Cryst Today*. 2005;14(4):1–15.
- [16] Lee SH, Park WS, Lee GD, et al. Low-cell-gap measurement by rotation of a wave retarder. *Jpn J Appl Phys*. 2002;41(1R):379.
- [17] Lien A, Takano H. Cell gap measurement of filled twisted nematic liquid crystal displays by a phase compensation method. *J Appl Phys*. 1991;69(3):1304–1309.
- [18] Tang ST, Kwok HS. Transmissive liquid crystal cell parameters measurement by spectroscopic ellipsometry. *J Appl Phys*. 2001;89(1):80–85.
- [19] Nakano F, Isogai M, Sato M. Simple method of determining liquid crystal tilt-bias angle. *Jpn J Appl Phys*. 1980;19(10):2013.
- [20] Vilfan M, Mertelj A, Čopič M. Dynamic light scattering measurements of azimuthal and zenithal anchoring of nematic liquid crystals. *Phys Rev E*. 2002;65(4):041712.
- [21] Barbero G, Madhusudana N, Durand G. Weak anchoring energy and pretilt of a nematic liquid crystal. *J Phys Lett*. 1984;45(12):613–619.
- [22] Nastishin YA, Polak R, Shiyankovskii SV, et al. Determination of nematic polar anchoring from retardation versus voltage measurements. *Appl Phys Lett*. 1999;75(2):202–204.

- [23] Murauski A, Chigrinov V, Muravsky A, et al. Determination of liquid-crystal polar anchoring energy by electrical measurements. *Phys Rev E*. 2005;71(6):061707.
- [24] Murauski A, Chigrinov V, Kwok HS. New method for measuring polar anchoring energy of nematic liquid crystals. *Liq Cryst*. 2009;36(8):779–786.
- [25] Pezzi L, Veltri A, De Luca A, et al. Model for molecular director configuration in a liquid crystal cell with multiple interfaces. *J Nonlinear Opt Phys Mater*. 2007;16(2):199–206.
- [26] Perivolari E, Gill J, Podoliak N, et al. Optically controlled bistable waveplates. *J Mol Liq*. 2018;267:484–489.
- [27] Dozov I, Stoenescu DN, Lamarque-Forget S, et al. Development of low anchoring strength liquid crystal mixtures for bistable nematic displays. *J Inf Disp*. 2005;6(3):1–5.
- [28] Shiyonovskii S, Lavrentovich O, Schneider T, et al. Lyotropic chromonic liquid crystals for biological sensing applications. *Mol Cryst Liq Cryst*. 2005;434(1):259/[587]-270/[598].
- [29] Sohn HR, Liu CD, Wang Y, et al. Light-controlled skyrmions and torons as reconfigurable particles. *Opt Express*. 2019;27(20):29055–29068.
- [30] Bennett T, Proctor M, Forster J, et al. Wide area mapping of liquid crystal devices with passive and active command layers. *Appl Opt*. 2017;56(32):9050–9056.
- [31] Bennett T, Proctor M, Kaczmarek M, et al. Lifting degeneracy in nematic liquid crystal viscosities with a single optical measurement. *J Colloid Interface Sci*. 2017;497:201–206.
- [32] Frank FCI. Liquid crystals. On the theory of liquid crystals. *Discuss Faraday Soc*. 1958;25:19–28.
- [33] Stewart IW. The static and dynamic continuum theory of liquid crystals: a mathematical introduction. London: Taylor & Francis; 2004.
- [34] Rapini A, Papoular M. Distorsion d'une lamelle nématique sous champ magnétique conditions d'ancrage aux parois. *J Phys Colloq*. 1969;30(C4):C4-54–C4-56.
- [35] Trefethen LN. Spectral methods in MATLAB, Software, Environments, and Tools. *Soc Ind Appl Math (SIAM)*. 2000;10.
- [36] Liu Y, Zhang Y, Oh BY, et al. Super-fast switching of liquid crystals sandwiched between highly conductive graphene oxide/dimethyl sulfate doped PEDOT: PSS composite layers. *J Appl Phys*. 2016;119(19):194505.
- [37] Chou TR, Chen SH, Chiang YT, et al. Highly conductive PEDOT: PSS films by post-treatment with dimethyl sulfoxide for ITO-free liquid crystal display. *J Mater Chem C*. 2015;3(15):3760–3766.
- [38] Wang X, Hu S, Li Q, et al. Inducting effects of ionic liquid crystal modified-PEDOT: PSS on the performance of bulk heterojunction polymer solar cells. *RSC Adv*. 2015;5(65):52874–52881.
- [39] Jeong S, Kwon Y, Choi BD, et al. Effects of nematic liquid crystal additives on the performance of polymer solar cells. *Macromol Chem Phys*. 2010;211(23):2474–2479.
- [40] Ericksen J. Anisotropic fluids. *Arch Ration Mech Anal*. 1959;4(1):231–237.
- [41] Barla G. Some constitutive equations for rock materials. The 11th US symposium on rock mechanics USRMS; University of California, Berkeley; American Rock Mechanics Association; 1969.
- [42] Regrettier T, Kaczmarek M, D'Alessandro G, et al. Integrated organic donor-acceptor bulk heterojunctions for self-activated liquid crystal light modulators. *Liq Cryst*. XXII; 2018; p. 1073514. International Society for Optics and Photonics.
- [43] Raynes E, Brown C, Strömer J. Method for the measurement of the K 22 nematic elastic constant. *Appl Phys Lett*. 2003;82(1):13–15.
- [44] Chen H, Zhu R, Zhu J, et al. A simple method to measure the twist elastic constant of a nematic liquid crystal. *Liq Cryst*. 2015;42(12):1738–1742.
- [45] Wang H, Wu TX, Gauza S, et al. A method to estimate the Leslie coefficients of liquid crystals based on MBBA data. *Liq Cryst*. 2006;33(1):91–98.
- [46] Yang F, Sambles J, Dong Y, et al. Fully leaky guided wave determination of the polar anchoring energy of a homogeneously aligned nematic liquid crystal. *J Appl Phys*. 2000;87(6):2726–2735.
- [47] Brimicombe P, Kischka C, Elston S, et al. Measurement of the twist elastic constant of nematic liquid crystals using pi-cell devices. *J Appl Phys*. 2007;101(4):043108.
- [48] Lin Y-H, Ren H, Wu YH, et al. Pinning effect on the phase separation dynamics of thin polymer-dispersed liquid crystals. *Opt Express*. 2005;13(2):468–474.
- [49] Seo DS, Iimura Y, Kobayashi S. Temperature dependence of the polar anchoring strength of weakly rubbed polyimide films for the nematic liquid crystal (5CB). *Appl Phys Lett*. 1992;61(2):234–236.
- [50] Seo DS, Kobayashi S, Kang DY, et al. Effects of rubbing and temperature dependence of polar anchoring strength of homogeneously aligned nematic liquid crystal on polyimide Langmuir-Blodgett orientation films. *Jpn J Appl Phys*. 1995;34(7R):3607.
- [51] Chigrinov VG, Kozenkov VM, Kwok H-S. Photoalignment of liquid crystalline materials: physics and applications. Vol. 17. John Wiley & Sons; US; 2008.
- [52] Nys I, Chen K, Beeckman J, et al. Periodic planar-homeotropic anchoring realized by photoalignment for stabilization of chiral superstructures. *Adv Opt Mater*. 2018;6:6.
- [53] Kiselev AD, Chigrinov V, Huang DD. Photoinduced ordering and anchoring properties of azo-dye films. *Phys Rev E*. 2005;72(6):061703.
- [54] Mavrona E, Mailis S, Podoliak N, et al. Intrinsic and photo-induced properties of high refractive index azobenzene based thin films. *Opt Mater Express*. 2018;8(2):420–430.